Available online at www.sciencedirect.com
ScienceDirect
International Journal of Solids and Structures 44 (2007) 3840–3860
INTERNATIONAL JOURNAL OF SOLIDS and STRUCTURES
www.elsevier.com/locate/ijsolstr

# A nodal integration technique for meshfree radial point interpolation method (NI-RPIM)

G.R. Liu [a,b], G.Y. Zhang [a,*], Y.Y. Wang [c], Z.H. Zhong [d], G.Y. Li [d], X. Han [d]

[a] *Centre for Advanced Computations in Engineering Science (ACES), Department of Mechanical Engineering, National University of Singapore, 9 Engineering Drive 1, Singapore 117576, Singapore*
[b] *The Singapore-MIT Alliance (SMA), E4-04-10, 4 Engineering Drive 3, Singapore 117576, Singapore*
[c] *Institute of High Performance Computing, Singapore 117528, Singapore*
[d] *State Key Laboratory of Advanced Technology for Vehicle Body Design and Manufacture, Hunan University, 410082, PR China*

Received 1 October 2005; received in revised form 21 October 2006
Available online 10 November 2006

**Abstract**

A novel nodal integration technique for the meshfree radial point interpolation method (NI-RPIM) is presented for solid mechanics problems. In the NI-RPIM, radial basis functions (RBFs) augmented with polynomials are used to construct shape functions that possess the Delta function property. Galerkin weak form is adopted for creating discretized system equations, in which nodal integration is used to compute system matrices. A stable and simple nodal integration scheme is proposed to perform the nodal integration numerically. The NI-RPIM is examined using a number of example problems including stress analysis of an automobile mechanical component. The effect of shape parameters and dimension of local support domain on the results of the NI-RPIM is investigated in detail through these examples. The numerical solutions show that the present method is a robust, reliable, stable meshfree method and possesses better computational properties compared with traditional linear FEM and original RPIM using Gauss integration scheme.


*Keywords:* Nodal integration; Meshfree; Meshless; Radial point interpolation; Stress analysis

## 1. Introduction

Meshfree methods have been developed and achieved remarkable progress in recent years. In general, meshfree methods can be categorized into three groups according to the formulation procedures used (Liu and Gu, 2005). The first category covers the meshfree methods based on strong forms of system equations, in which discretization is performed directly from the governing differential equations, such as the general

* Corresponding author. Tel.: +65 6516 4796; fax: +65 6516 1459.
*E-mail address:* g0203729@nus.edu.sg (G.Y. Zhang).
*URL:* http://www.nus.edu.sg/ACES (G.Y. Zhang).

0020-7683/$ - see front matter © 2006 Elsevier Ltd. All rights reserved.
doi:10.1016/j.ijsolstr.2006.10.025

finite difference method (Liszka and Orkisz, 1980), the smooth particle hydrodynamic (SPH) method (Lucy, 1977; Liu and Liu, 2003) and other meshfree collocation methods. The second category includes the meshfree methods based on weak forms of system equations, such as the element-free Galerkin (EFG) method (Belytschko et al., 1994), the meshless local Petrov-Galerkin (MLPG) method (Atluri and Zhu, 1998), the point interpolation method (PIM) (Liu and Gu, 2001; Liu, 2002) etc. The third category concerns meshfree methods based on the combination of weak and strong forms, such as the meshfree weak–strong-form (MWS) method (Liu and Gu, 2003; Liu et al., 2004).

Two types of PIM formulations using the polynomial basis and the radial basis function (RBF) have been formulated so far (Liu and Gu, 2001; Wang and Liu, 2002a). In the meshfree radial point interpolation method (RPIM), RBFs augmented with polynomials and nodes in the local support domain are used to construct shape functions and the Galerkin weak form is adopted to derive a set of discrete system equations. The shape functions so constructed possess the Delta function property, which allows straightforward imposition of point essential boundary conditions, and many numerical techniques used in FEM can be applied in the RPIM with minimum modifications. Compared with meshfree methods based on strong form formulations, meshfree methods based on weak forms can usually achieve higher accuracy and results are very stable. This is due to the use of integration that provides smooth operations to the system. On the other hand, however, meshfree weak form methods can be more expensive because the integration needs to be performed numerically. In addition, background cells are also required for such numerical integrations.

Gauss integration scheme is commonly used for the numerical integration of meshfree weak form methods, which is very similar to that in the FEM. However, some nodal integration techniques have been suggested for the integration of weak form methods (Belytschko and Beissel, 1996; Chen et al., 2001). In this work, we attempt to develop an alternative, stable and simply nodal integration (NI) technique for meshfree weak form methods and it is implemented in the process of numerical integration for the RPIM. As direct nodal integration would often cause the phenomenon of instability, Taylor's expansion is used to serve as the stabilization terms, which have been studied for FEM (Liu et al., 1985) and other meshfree methods (Liu et al., 1996; Nagashima, 1999). In Nagashima's work, the formulation is based on EFG method that uses MLS shape functions and first-order of Taylor series expansion to the strain matrix is employed for stabilization. In the present work, the formulation is based on RPIM, the expansion is applied to the entirety of $\mathbf{B}^{\mathrm{T}}\mathbf{D}\mathbf{B}$ and it is expanded up to second-order. In this case, third-order derivatives of shape functions are required for linear elasticity problems. The RPIM shape functions created using RBFs fits well to the requirement, as it is one-piecely differentiable to any order in the integration domain (Liu, 2002). It is also noted that the expansion of $\mathbf{B}^{\mathrm{T}}\mathbf{D}\mathbf{B}$ to second-order is crucial, because the first-order term will vanish for symmetrical integral domain and has no stabilization effect. The method so constructed is called NI-RPIM and is examined in detail using a number of benchmark examples, and applied to stress analysis of an automotive component. This integral scheme is formulated based on the simple Taylor series expansion and hence it is very easy to implement in any meshfree weak form method for stable nodal integration.

The outline of this paper is as follows: in Section 2, the procedure leading to RPIM shape functions is briefly introduced. Section 3 briefs basic equations including the Galerkin weak form. In Section 4, a novel nodal integration technique based on the Taylor series expansion is presented for 1D and 2D problems. In Section 5, some 1D and 2D numerical examples are examined to study the accuracy, stability and efficiency of the present method, and the applicability to problems of complex geometry. Finally, Section 6 concludes this work.

## 2. RPIM shape functions

Radial basis functions (RBFs) are useful for function approximation based on arbitrary distributed nodes (Powell, 1992), and RPIM shape functions can be created using RBFs for meshfree methods following a simple procedure given for example (Liu, 2002). A field function $u(\mathbf{x})$ is first approximated as follows using RBFs augmented with polynomials in the local support domain of the point of interest.

$$u(\mathbf{x}) = \sum_{i=1}^{n} R_i(\mathbf{x}) a_i + \sum_{j=1}^{m} P_j(\mathbf{x}) b_j = \mathbf{R}^{\mathrm{T}}(\mathbf{x})\mathbf{a} + \mathbf{P}^{\mathrm{T}}(\mathbf{x})\mathbf{b}, \tag{1}$$

where $R_i(\mathbf{x})$ and $P_j(\mathbf{x})$ are radial basis functions and polynomial basis functions, respectively, $a_i$ and $b_j$ are corresponding constants, $n$ is the number of field nodes in the local support domain and $m$ is the number of polynomial terms.

There are several types of RBFs, and the multi-quadrics (MQ) (Hardy, 1990) is adopted in this work. The MQ-RBF is a function of nodal distance $r_i$ defined as follows (Liu, 2002):

$$R_i(\mathbf{x}) = (r_i^2 + (\alpha_c d_c)^2)^q, \tag{2}$$

where $d_c$ is the average nodal spacing near the point of interest $\mathbf{x}$; $\alpha_c$ and $q$ are two arbitrary real numbers of dimensionless parameters, and

$$r_i = \sqrt{(x - x_i)^2 + (y - y_i)^2}. \tag{3}$$

The polynomial basis function usually has the following terms,

$$\mathbf{P}^{\mathrm{T}}(\mathbf{x}) = \{1, x, y, x^2, xy, y^2, \ldots\}. \tag{4}$$

In this study, linear polynomials are used in the augmentation.

To perform the interpolation, a local support domain of the point of interest will be taken and the field values at the nodes in this domain will be used to implement the interpolation. In this work, a circular domain centered at the point of interest is adopted. The dimension of the local support domain, defined as the radius of the circle, is given by,

$$d_s = \alpha_s d_c, \tag{5}$$

where $\alpha_s$ is a positive real number of dimensionless size of the local support domain.

Constants $a_i$ and $b_j$ in Eq. (1) can be determined by enforcing the field function pass through all $n$ field nodes in the local support domain. At the $k$th point, it has the following form:

$$u(x_k, y_k) = \sum_{i=1}^{n} R_i(x_k, y_k) a_i + \sum_{j=1}^{m} P_j(x_k, y_k) b_j, \quad k = 1, 2, \ldots, n. \tag{6}$$

The matrix form of the above equation can be expressed as

$$\mathbf{U}_e = \mathbf{R}_q \mathbf{a} + \mathbf{P}_m \mathbf{b}. \tag{7}$$

where $\mathbf{U}_e$ is the vector of function values at the nodes in the local support domain

$$\mathbf{U}_e = \{ u_1 \quad u_2 \quad \ldots \quad u_n \}^{\mathrm{T}}. \tag{8}$$

$\mathbf{R}_q$ is the moment matrix of RBFs,

$$\mathbf{R}_q = \begin{bmatrix} R_1(r_1) & R_2(r_1) & \ldots & R_n(r_1) \\ R_1(r_2) & R_2(r_2) & \ldots & R_n(r_2) \\ \ldots & \ldots & \ldots & \ldots \\ R_1(r_n) & R_2(r_n) & \ldots & R_n(r_n) \end{bmatrix}_{(n \times n)} \tag{9}$$

$\mathbf{P}_m$ is the polynomial moment matrix,

$$\mathbf{P}_m = \begin{bmatrix} 1 & x_1 & y_1 & \ldots & p_m(\mathbf{x}_1) \\ 1 & x_2 & y_2 & \ldots & p_m(\mathbf{x}_2) \\ \ldots & \ldots & \ldots & \ldots & \ldots \\ 1 & x_n & y_n & \ldots & p_m(\mathbf{x}_n) \end{bmatrix}_{(n \times m)} \tag{10}$$

$\mathbf{a}$ is the vector of unknown coefficients for RBFs,

$$\mathbf{a}^{\mathrm{T}} = \{ a_1 \quad a_2 \quad \ldots \quad a_n \} \tag{11}$$

**b** is the vector of unknown coefficients for polynomial basis functions,

$$\mathbf{b}^{\mathrm{T}} = \{\, b_1 \quad b_2 \quad \dots \quad b_m \,\}. \tag{12}$$

To obtain unique solutions of Eq. (7), the constraint conditions should be applied as follows (Golberg et al., 1999),

$$\sum_{i=1}^{n} p_j(\mathbf{x}_i) a_i = \mathbf{P}_m^{\mathrm{T}} \mathbf{a} = 0, \quad j = 1, 2, \dots, m. \tag{13}$$

Combination of Eqs. (7) and (13) yields the following equations in the matrix form:

$$\tilde{\mathbf{U}}_e = \begin{bmatrix} \mathbf{U}_e \\ \mathbf{0} \end{bmatrix} = \begin{bmatrix} \mathbf{R}_q & \mathbf{P}_m \\ \mathbf{P}_m^T & \mathbf{0} \end{bmatrix} \begin{Bmatrix} \mathbf{a} \\ \mathbf{b} \end{Bmatrix} = \mathbf{G}\mathbf{a}_0, \tag{14}$$

where

$$\tilde{\mathbf{U}}_e = \begin{bmatrix} \mathbf{U}_e \\ \mathbf{0} \end{bmatrix} = \{\, u_1 \quad u_2 \quad \dots \quad u_n \quad 0 \quad 0 \quad \dots \quad 0 \,\}^{\mathrm{T}}. \tag{15}$$

Unique solution is obtained if the inverse of matrix **G** exists:

$$\mathbf{a}_0 = \begin{Bmatrix} \mathbf{a} \\ \mathbf{b} \end{Bmatrix} = \mathbf{G}^{-1} \tilde{\mathbf{U}}_e. \tag{16}$$

Note that $\mathbf{R}_q^{-1}$ usually exists for arbitrarily scattered nodes (Hardy, 1990; Schaback, 1994; Wendland, 1998). Therefore, there is no singularity problem in the RPIM because only a small number of nodes (usually 10–40 for 2D problems) are used in the local support domain (Liu, 2002; Liu and Gu, 2005).

Substituting Eq. (16) into Eq. (1), the interpolation can be expressed as

$$u(\mathbf{x}) = \left\{\, \mathbf{R}^{\mathrm{T}}(\mathbf{x}) \quad \mathbf{P}^{\mathrm{T}}(\mathbf{x}) \,\right\} \mathbf{G}^{-1} \tilde{\mathbf{U}}_e = \tilde{\Phi}(\mathbf{x}) \tilde{\mathbf{U}}_e. \tag{17}$$

Finally, the RPIM shape functions for the corresponding $n$ field nodes can be obtained as

$$\Phi^{\mathrm{T}}(\mathbf{x}) = \{\, \phi_1(\mathbf{x}) \quad \phi_2(\mathbf{x}) \quad \dots \quad \phi_n(\mathbf{x}) \,\}. \tag{18}$$

The approximation function can be written as

$$u(\mathbf{x}) = \Phi^{\mathrm{T}}(\mathbf{x}) \mathbf{U}_e = \sum_{i=1}^{n} \phi_i u_i. \tag{19}$$

The derivatives of $u(\mathbf{x})$ can be easily obtained as

$$u_{,k}(\mathbf{x}) = \Phi_{,k}^{\mathrm{T}}(\mathbf{x}) \mathbf{U}_e, \tag{20}$$

where $k$ denotes the coordinates $x$ or $y$. A comma designates a partial differentiation with respect to the indicated spatial coordinate that follows.

## 3. Galerkin weak form

Consider a two-dimensional solid problem defined in domain $\Omega$ bounded by $\Gamma$ ($\Gamma = \Gamma_t + \Gamma_u$), the governing equations of this problem can be expressed as follows (Timoshenko and Goodier, 1970).

Equilibrium equation:

$$\mathbf{L}^{\mathrm{T}} \boldsymbol{\sigma} + \mathbf{b} = 0 \quad \text{in } \Omega. \tag{21}$$

Natural and essential boundary conditions:

$$\boldsymbol{\sigma} \cdot \mathbf{n} = \bar{\mathbf{t}} \quad \text{on } \Gamma_t \tag{22}$$

$$\mathbf{u} = \bar{\mathbf{u}} \quad \text{on } \Gamma_u, \tag{23}$$

where $\mathbf{L}^{\mathrm{T}} = \begin{bmatrix} \frac{\partial}{\partial x} & 0 & \frac{\partial}{\partial y} \\ 0 & \frac{\partial}{\partial y} & \frac{\partial}{\partial x} \end{bmatrix}$ is differential operator; $\boldsymbol{\sigma}^{\mathrm{T}} = \{ \sigma_{xx} \quad \sigma_{yy} \quad \tau_{xy} \}$ is the stress vector, $\mathbf{u}^{\mathrm{T}} = \{ u \quad v \}$ is the displacement vector, $\mathbf{b}^{\mathrm{T}} = \{ b_x \quad b_y \}$ is the body force vector, $\bar{\mathbf{t}}$ is the prescribed traction on the natural boundaries, $\bar{\mathbf{u}}$ is the prescribed displacement on the essential boundaries, and $\mathbf{n}$ is the vector of unit outward normal at a point on the natural boundary.

The unconstrained Galerkin weak form of Eq. (21) is presented as follows (Liu, 2002):

$$\int_{\Omega} (\mathbf{L}\delta\mathbf{u})^{\mathrm{T}} (\mathbf{D}\mathbf{L}\mathbf{u}) \, \mathrm{d}\Omega - \int_{\Omega} \delta\mathbf{u}^{\mathrm{T}} \mathbf{b} \, \mathrm{d}\Omega - \int_{\Gamma_t} \delta\mathbf{u}^{\mathrm{T}} \mathbf{t} \, \mathrm{d}\Gamma = 0. \tag{24}$$

For linear elasticity, the material matrix $\mathbf{D}$ is expressed as follows:

$$\begin{aligned} \mathbf{D} &= \frac{E}{1-v^2} \begin{bmatrix} 1 & v & 0 \\ v & 1 & 0 \\ 0 & 0 & \frac{1-v}{2} \end{bmatrix} \quad \text{for plane stress problem,} \\ \mathbf{D} &= \frac{E(1-v)}{(1+v)(1-2v)} \begin{bmatrix} 1 & \frac{v}{1-v} & 0 \\ \frac{v}{1-v} & 1 & 0 \\ 0 & 0 & \frac{1-2v}{2(1-v)} \end{bmatrix} \quad \text{for plane strain problem,} \end{aligned} \tag{25}$$

where $E$ is Young's modulus and $v$ is Poisson's ratio.

Substituting the approximation equation Eq. 19 into Eq. (24) yields,

$$\mathbf{K}\mathbf{u} = \mathbf{f}, \tag{26}$$

where

$$\mathbf{K}_{ij} = \int_{\Omega} \mathbf{B}_i^{\mathrm{T}} \mathbf{D} \mathbf{B}_j \, \mathrm{d}\Omega, \tag{27}$$

$$\mathbf{f}_i = \int_{\Gamma_t} \phi_i \bar{\mathbf{t}} \, \mathrm{d}\Gamma + \int_{\Omega} \phi_i \mathbf{b} \, \mathrm{d}\Omega, \tag{28}$$

$$\mathbf{B}_i = \begin{bmatrix} \phi_{i,x} & 0 \\ 0 & \phi_{i,y} \\ \phi_{i,y} & \phi_{i,x} \end{bmatrix}. \tag{29}$$

## 4. A nodal integration technique

Consider now an integral,

$$I = \int_{\Omega} f(\mathbf{x}) \, \mathrm{d}\Omega, \tag{30}$$

where $f(\mathbf{x})$ is an arbitrary function integrable, which is, for example, a component of matrix $\mathbf{B}_i^{\mathrm{T}} \mathbf{D} \mathbf{B}_j$ given in Eq. (27); $\Omega$ is the domain of the problem, that is represented by a set of $N$ nodes distributed in the problem domain.

In a nodal integration scheme, the domain $\Omega$ is divided into a set of non-overlapping sub-domains $\Omega_i (i = 1, 2, \ldots, N)$, each of them includes a node, and $\Omega = \sum_{i=1}^{N} \Omega_i$. Then the integration, Eq. (30), can then be expressed as

$$I = \sum_{i=1}^{N} \int_{\Omega_i} f(\mathbf{x}) \, \mathrm{d}\Omega_i. \tag{31}$$

In a meshfree method based on weak form, a background mesh is needed for the implementation of numerical integration. For the present method, a background mesh is used for constructing the nodal integration domain

for each node. The background mesh is not used for shape function construction which is constructed using a same set of nodes located in a local support domain. The free of mesh from shape function construction has many advantages including the improvement in accuracy, which will be observed later in examples. This fact has also been found in many other existing works (Belytschko et al., 1994; Atluri and Zhu, 1998; Chen et al., 2001). It is very clear that one does not have to use mesh for shape function construction. In the present work, the mesh is also only used for integration purpose.

The question now is how to evaluate $\int_{\Omega_i} f(\mathbf{x})\,\mathrm{d}\Omega_i$ over the nodal integration domain $\Omega_i$. Here we present a novel and simple approach based on the Taylor series extension. The basic idea of this approach is to extend the integral function into some terms of Taylor series, and the integration will be approximately performed on these terms. Note that the integrand $f(\mathbf{x})$ is required to be differentiable within the integration domain when it is extended to be terms of Taylor series. Therefore, we construct RPIM shape functions using the same set of nodes in each integration domain. A shape function so constructed is one-piece, and hence is differentiable to any order in the integration domain. Note that the discontinuity will occur on the interfaces of the integration domains, and hence causes the non-conformability, which is omitted in this work, as it is controlled by the use of RBF shape functions with proper shape parameters (Liu, 2002). Note that this kind of non-conformability exists for all the meshfree methods based on weak form and nodal integration even the ones using MLS shape functions, unless strain smoothing technique is used (Chen et al., 2001; Liu et al., 2005a; Liu et al., 2006).

For comparison, the EFG method based on the present nodal integration scheme is also coded, in which shape functions are obtained using the MLS method (Belytschko et al., 1994). For convenience in this paper, we label this method as NI-MLS. It is known that the MLS shape functions can be constructed to satisfy the compatibility condition and the continuity of the field function approximation is ensured (Liu, 2002).

### 4.1. Nodal integration technique for 1D problems

To explain our method more clearly, we start with one-dimensional problems. Based on Taylor series extension, a continuous function $f(x)$ can be approximated in the vicinity of a point $x_0$ as follows:

$$f(x) \approx f(x_0) + f'(x_0)x + \frac{f''(x_0)}{2!}x^2, \tag{32}$$

where the third-order and above are truncated.

The integration for the function $f(x)$ in the domain $(x_1 \leqslant x \leqslant x_2)$ can then be evaluated as,

$$\begin{aligned}\int_{x_1}^{x_2} f(x)\,\mathrm{d}x &\approx \int_{x_1}^{x_2} \left(f(x_0) + f'(x_0)x + \frac{1}{2}f''(x_0)x^2\right)\mathrm{d}x \\ &= \int_{x_1}^{x_2} f(x_0)\,\mathrm{d}x + \int_{x_1}^{x_2} f'(x_0)x\,\mathrm{d}x + \frac{1}{2}\int_{x_1}^{x_2} f''(x_0)x^2\,\mathrm{d}x \\ &= f(x_0)(x_2 - x_1) + \frac{1}{2}f'(x_0)(x_2^2 - x_1^2) + \frac{1}{6}f''(x_0)(x_2^3 - x_1^3).\end{aligned} \tag{33}$$

Considering now a one-dimensional (1D) problem to be solved using RPIM. The problem domain is presented by a set of nodes, as shown in Figs. 1 and 2. The integrand of $f(x)$ is now a component of the matrix $\mathbf{B}_i^T\mathbf{D}\mathbf{B}_j$ (see Eq. (27)). When the field nodes are regularly distributed, by using Eq. (33), the numerical integration for the $i$th node can be performed as follows.

For an internal node, we obtain

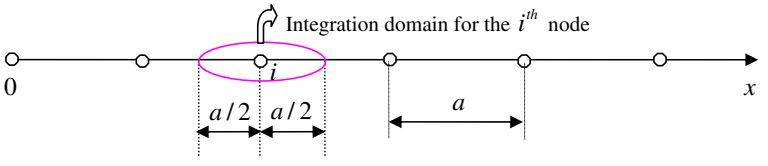


Fig. 1. Nodal integration domain for regularly distributed nodes for 1D problem.

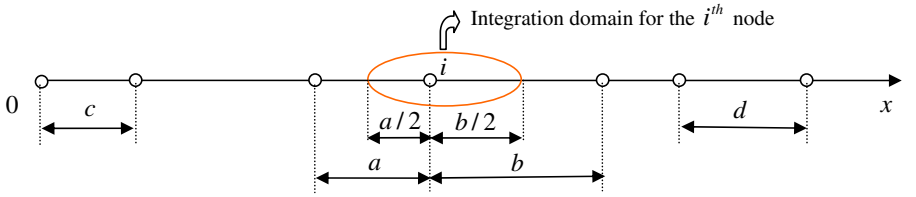


Fig. 2. Nodal integration domain for irregularly distributed nodes for 1D problem.

$$\int_{-\frac{a}{2}}^{\frac{a}{2}} f(x)\,dx = f(x_i)\left(\frac{a}{2}+\frac{a}{2}\right)+\frac{1}{2}f'(x_i)\left[\left(\frac{a}{2}\right)^2-\left(-\frac{a}{2}\right)^2\right]+\frac{1}{6}f''(x_i)\left[\left(\frac{a}{2}\right)^3-\left(-\frac{a}{2}\right)^3\right]$$
$$= f(x_i)a+0+\frac{1}{24}f''(x_i)a^3, \tag{34}$$

where $a$ is the nodal spacing as shown in Fig. 1.

For the node located at the left end of the 1D domain, we have

$$\int_{0}^{\frac{a}{2}} f(x)\,dx = f(x_i)\left(\frac{a}{2}-0\right)+\frac{1}{2}f'(x_i)\left[\left(\frac{a}{2}\right)^2-0\right]+\frac{1}{6}f''(x_i)\left[\left(\frac{a}{2}\right)^3-0\right]$$
$$= \frac{1}{2}f(x_i)a+\frac{1}{8}f'(x_i)a^2+\frac{1}{48}f''(x_i)a^3. \tag{35}$$

For the node located at the right end of the 1D domain,

$$\int_{\frac{a}{2}}^{0} f(x)\,dx = f(x_i)\left(0+\frac{a}{2}\right)+\frac{1}{2}f'(x_i)\left[0-\left(\frac{a}{2}\right)^2\right]+\frac{1}{6}f''(x_i)\left[0-\left(-\frac{a}{2}\right)^3\right]$$
$$= \frac{1}{2}f(x_i)a-\frac{1}{8}f'(x_i)a^2+\frac{1}{48}f''(x_i)a^3. \tag{36}$$

When the field nodes are irregularly distributed, Eqs. (34)–(36) can be expressed as follows.

For an internal node:

$$\int_{-\frac{a}{2}}^{\frac{b}{2}} f(x)\,dx = f(x_i)\left(\frac{b}{2}+\frac{a}{2}\right)+\frac{1}{2}f'(x_i)\left[\left(\frac{b}{2}\right)^2-\left(-\frac{a}{2}\right)^2\right]+\frac{1}{6}f''(x_i)\left[\left(\frac{b}{2}\right)^3-\left(-\frac{a}{2}\right)^3\right]$$
$$= \frac{1}{2}f(x_i)(a+b)+\frac{1}{8}f'(x_i)(b^2-a^2)+\frac{1}{48}f''(x_i)(a^3+b^3). \tag{37}$$

For the node located at the left end of the 1D domain:

$$\int_{0}^{\frac{c}{2}} f(x)\,dx = f(x_i)\left(\frac{c}{2}-0\right)+\frac{1}{2}f'(x_i)\left[\left(\frac{c}{2}\right)^2-0\right]+\frac{1}{6}f''(x_i)\left[\left(\frac{c}{2}\right)^3-0\right]$$
$$= \frac{1}{2}f(x_i)c+\frac{1}{8}f'(x_i)c^2+\frac{1}{48}f''(x_i)c^3. \tag{38}$$

For the node located at the right end of the 1D domain:

$$\int_{-\frac{d}{2}}^{0} f(x)\,dx = f(x_i)\left(0+\frac{d}{2}\right)+\frac{1}{2}f'(x_i)\left[0-\left(-\frac{d}{2}\right)^2\right]+\frac{1}{6}f''(x_i)\left[0-\left(-\frac{d}{2}\right)^3\right]$$
$$= \frac{1}{2}f(x_i)d-\frac{1}{8}f'(x_i)d^2+\frac{1}{48}f''(x_i)d^3, \tag{39}$$

where $a$, $b$, $c$ and $d$ are nodal spacing for the irregularly distributed nodes as shown in Fig. 2.

### 4.2. Nodal integration technique for 2D problems

Applying Taylor series extension, a two-dimensional (2D) continuous function $f(x,y)$ can be approximated in the vicinity of point $(x_0,y_0)$ as follows:

$$f(x,y) \approx f(x_0,y_0) + \left(x\frac{\partial}{\partial x} + y\frac{\partial}{\partial y}\right) f(x_0,y_0) + \frac{1}{2!}\left(x\frac{\partial}{\partial x} + y\frac{\partial}{\partial y}\right)^2 f(x_0,y_0). \tag{40}$$

The integration for function $f(x,y)$ over the nodal integration domain $\Omega_i$ can be expressed as

$$\begin{aligned}
\int\int_{\Omega_i} f(x,y)\,\mathrm{d}\Omega &\approx \int\int_{\Omega_i} \left( f(x_0,y_0) + \left(x\frac{\partial}{\partial x} + y\frac{\partial}{\partial y}\right) f(x_0,y_0) + \frac{1}{2!}\left(x\frac{\partial}{\partial x} + y\frac{\partial}{\partial y}\right)^2 f(x_0,y_0) \right) \mathrm{d}\Omega \\
&= f(x_0,y_0)\int\int_{\Omega_i} 1\,\mathrm{d}\Omega + f_{,x}(x_0,y_0)\int\int_{\Omega_i} x\,\mathrm{d}\Omega + f_{,y}(x_0,y_0)\int\int_{\Omega_i} y\,\mathrm{d}\Omega \\
&\quad + \frac{1}{2}f_{,xx}(x_0,y_0)\int\int_{\Omega_i} x^2\,\mathrm{d}\Omega + f_{,xy}(x_0,y_0)\int\int_{\Omega_i} xy\,\mathrm{d}\Omega + \frac{1}{2}f_{,yy}(x_0,y_o)\int\int_{\Omega_i} y^2\,\mathrm{d}\Omega \\
&= f(x_0,y_0)A_i + f_{,x}(x_0,y_0)M_{yi} + f_{,y}(x_0,y_0)M_{xi} \\
&\quad + \frac{1}{2}f_{,xx}(x_0,y_0)M_{yyi} + f_{,xy}(x_0,y_0)M_{xyi} + \frac{1}{2}f_{,yy}(x_0,y_0)M_{xxi},
\end{aligned} \tag{41}$$

where $A_i$ is the area of the nodal integration domain of the $i$th node,

$$M_{xi} = \int\int_{A_i} y\,\mathrm{d}A_i \quad M_{yi} = \int\int_{A_i} x\,\mathrm{d}A_i \tag{42}$$

are the area moments of first-order for the integration domain of the $i$th node, and

$$M_{xxi} = \int\int_{A_i} y^2\,\mathrm{d}A_i, \quad M_{yyi} = \int\int_{A_i} x^2\,\mathrm{d}A_i, \quad M_{xyi} = \int\int_{A_i} xy\,\mathrm{d}A_i \tag{43}$$

are the area moments of second-order for the integration domain of the $i$th node.

The integration for function $f(x,y)$ along the boundary line can be formulated as

$$\begin{aligned}
\int_\Gamma f(x,y)\,\mathrm{d}l &= \int_\Gamma \left( f(x_0,y_0) + \left(x\frac{\partial}{\partial x} + y\frac{\partial}{\partial y}\right) f(x_0,y_0) + \frac{1}{2!}\left(x\frac{\partial}{\partial x} + y\frac{\partial}{\partial y}\right)^2 f(x_0,y_0) \right) \mathrm{d}l \\
&= f(x_0,y_0)\int_\Gamma 1\,\mathrm{d}l + f_{,x}(x_0,y_0)\int_\Gamma x\,\mathrm{d}l + f_{,y}(x_0,y_0)\int_\Gamma y\,\mathrm{d}l \\
&\quad + \frac{1}{2}f_{,xx}(x_0,y_0)\int_\Gamma x^2\,\mathrm{d}l + f_{,xy}(x_0,y_0)\int_\Gamma xy\,\mathrm{d}l + \frac{1}{2}f_{,yy}(x_0,y_o)\int_\Gamma y^2\,\mathrm{d}l.
\end{aligned} \tag{44}$$

To apply the nodal integration technique, a background cell is needed to divide the problem domain into nodal integration domains, each of which includes a node. When the nodes are regularly distributed, a rectangular domain can be used as the nodal integration domain $\Omega_i$ (illustrated in Fig. 3), and the union of all the rectangles forms the problem domain. As shown in Fig. 4, when the nodes are irregularly distributed, a tessellation can always be generated automatically by joining the centroids of the triangles and the mid-edge points (Ferziger and Peric, 1999).

According to Eq. (41), the area $A_i$ and the moments $M_{xi}$, $M_{yi}$, $M_{xxi}$, $M_{yyi}$ and $M_{xyi}$ for the $i$th field node can be calculated during the pre-process stage for later use in the numerical integration, because they depend on only the geometry of the nodal integration domain.

## 5. Numerical examples

Several numerical examples are studied in this section. The materials used in the examples are all linear elastic with Young's modulus $E = 3.0 \times 10^7$ and poisson's ratio $v = 0.3$. The units used in this paper can be any

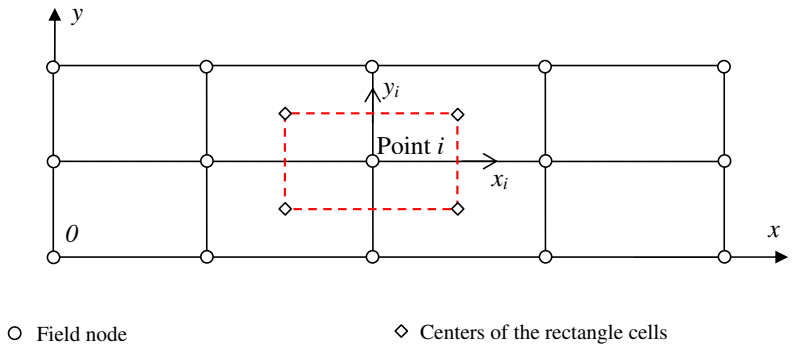


Fig. 3. Illustration of rectangular background cells and integral domain for the $i$th node in two dimensions.

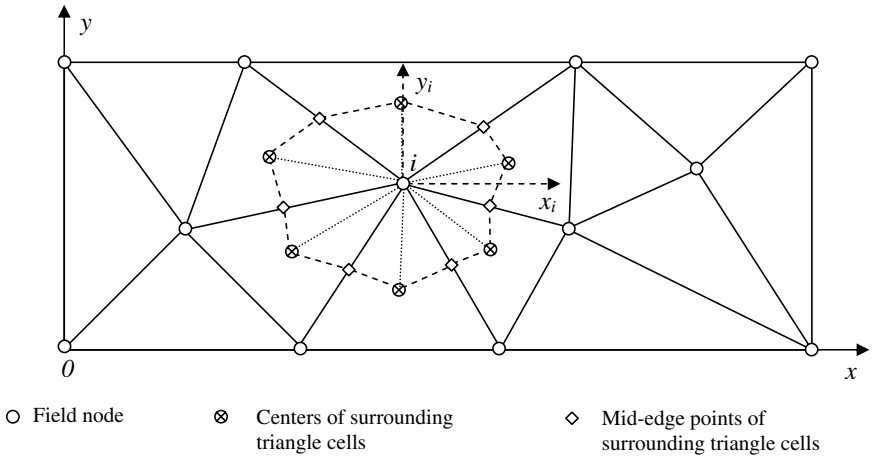


Fig. 4. Illustration of triangular background cells and the integral domain for the $i$th node in two dimensions.

consistent unit based on international standard unit system. The error indicators in displacement and energy are, respectively, defined as follows:

$$E_d = \sqrt{\frac{\sum_{i=1}^{N}\left(u_i^{\text{exact}} - u_i^{\text{numerical}}\right)^2}{\sum_{i=1}^{n}\left(u_i^{\text{exact}}\right)^2}} \tag{45}$$

$$E_e = \frac{1}{A}\sqrt{\frac{1}{2}\int_{\Omega}\left(\boldsymbol{\varepsilon}^{\text{exact}} - \boldsymbol{\varepsilon}^{\text{numerical}}\right)^{\mathrm{T}}\mathbf{D}\left(\boldsymbol{\varepsilon}^{\text{exact}} - \boldsymbol{\varepsilon}^{\text{numerical}}\right)\mathrm{d}\Omega}, \tag{46}$$

where the superscript exact notes the exact or analytical solution, numerical notes a numerical solution obtained using a numerical method including the present NI-RPIM, and $A$ is the area of the problem domain.

### 5.1. A one-dimension bar subjected to body force

A simple benchmark problem of 1D bar subjected to body force is studied first. The governing equation and the boundary conditions are shown as follows:

$$E\frac{\partial^2 u(x)}{\partial x^2} + 10x = 0 \quad (0 \leqslant x \leqslant 10), \tag{47}$$

$$u(0) = 0, \quad u(10) = 0. \tag{48}$$

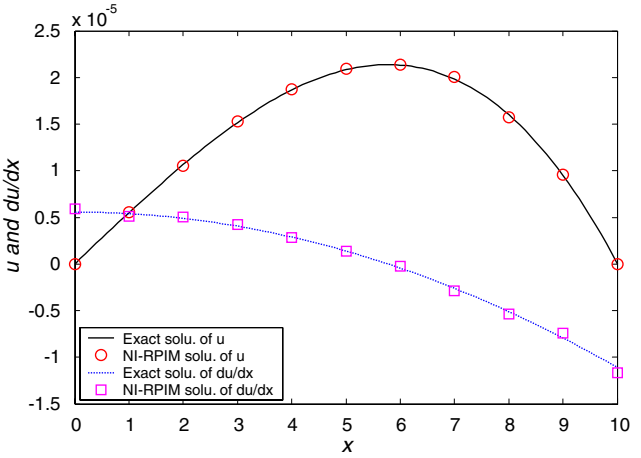


Fig. 5. Exact and numerical solutions of $u$ and $\mathrm{d}u/\mathrm{d}x$ for the one-dimensional bar problem.

The analytical solution of this simple problem has the following polynomial form:

$$u(x) = -\frac{5}{3E}x^3 + \frac{500}{3E}x. \tag{49}$$

In this study, 11 regularly distributed nodes are adopted. Solutions of field function $u$ and its derivative $\mathrm{d}u/\mathrm{d}x$ are first obtained using the present method, and compared with the analytical solutions, as shown in Fig. 5. It shows that the numerical solutions of both the function values and their first-order derivatives are in good agreement with the analytical solutions.

### 5.2. A one-dimensional problem with non-polynomial solution

In this study, the following problem is considered:

$$\frac{\mathrm{d}^2u}{\mathrm{d}x^2} + 25u = 0 \quad (0 \leqslant x \leqslant 1), \tag{50}$$

$$u_{,x}(0) = u_{,x}(1) = 1. \tag{51}$$

The exact solution of $u(x)$ can be easily found as follows:

$$u(x) = \frac{\cos 5 - 1}{5 \sin 5}\cos 5x + \frac{1}{5}\sin 5x \tag{52}$$

which is not in polynomial form.

The numerical solutions of $u(x)$ and $\mathrm{d}u(x)/\mathrm{d}x$ are obtained using the present method with eleven regularly distributed nodes, and the results are shown in Figs. 6 and 7 together with the analytical solutions. A very good agreement is again observed. A convergence study is also performed by using seven different nodal densities (4, 7, 13, 25, 49, 97 and 193 regular nodes). The error results of function value computed using Eq. (45) is shown in Fig. 8. and the convergence rate is about 1.94.

### 5.3. A cantilever beam

A benchmark problem of 2D cantilever beam in Fig. 9 is now studied. The beam is of length $L$, height $D$ and subjected to parabolic traction at the free end. As the beam has a unit thickness, it can be taken as a plane stress problem and the analytical solutions of displacement and stress components are shown as follows (Timoshenko and Goodier, 1970),

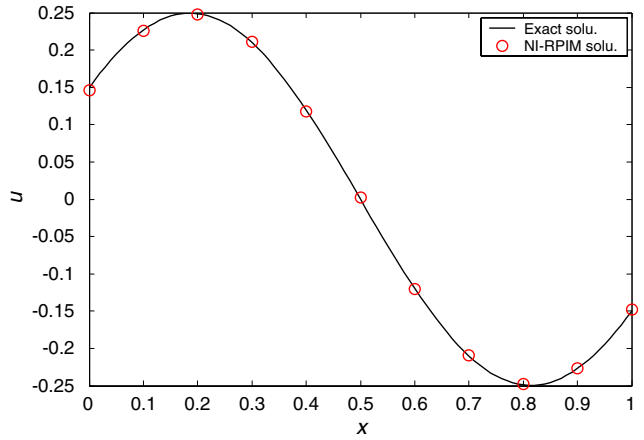


Fig. 6. Exact and numerical solutions of $u$ for the one-dimensional problem with trigonometric form of solution.

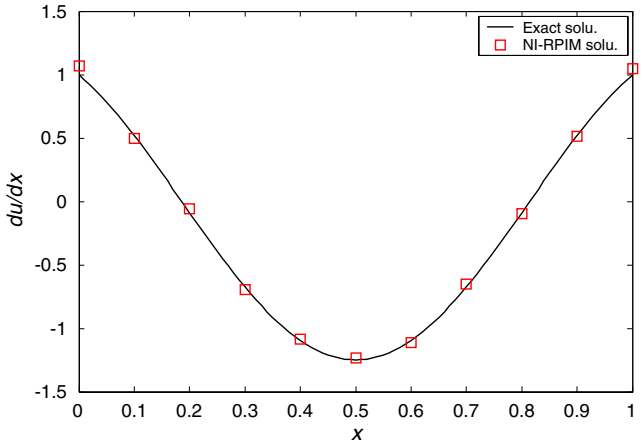


Fig. 7. Exact and numerical solutions of d$u$/d$x$ for the one-dimensional problem with trigonometric form of solutions.

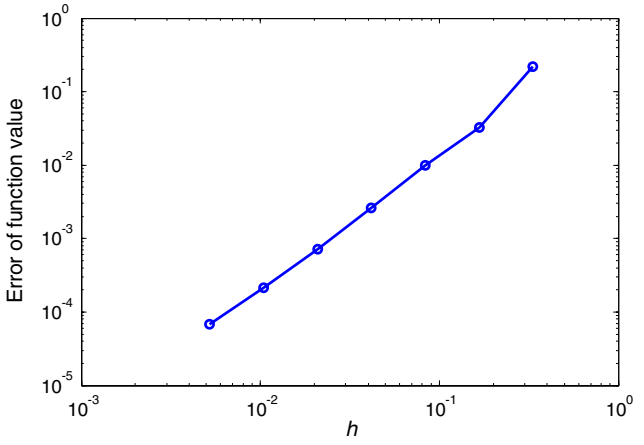


Fig. 8. The convergence study of the present method by using the one-dimensional bar problem (The convergence rate is about 1.94).

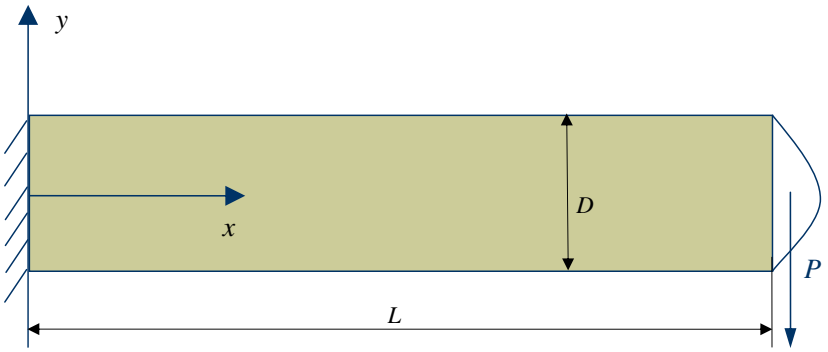


Fig. 9. Cantilever beam subjected to a parabolic traction at the free end.

$$u_x = -\frac{py}{6EI}\left[(6L-3x)x + (2+v)\left(y^2 - \frac{D^2}{4}\right)\right], \tag{53}$$

$$u_y = \frac{p}{6EI}\left[3vy^2(L-x) + (4+5v)\frac{D^2x}{4} + (3L-x)x^2\right], \tag{54}$$

where the moment of the inertia of the beam is given as $I = D^3/12$.

The stress components corresponding to above displacements are as,

$$\sigma_x = -\frac{p(L-x)y}{I}, \tag{55}$$

$$\sigma_y = 0, \tag{56}$$

$$\sigma_{xy} = \frac{p}{2I}\left[\frac{D^2}{4} - y^2\right]. \tag{57}$$

The values of the parameters are taken as: $L = 50$, $D = 10$ and $p = -1000$.

*5.3.1. Effect of shape parameters*

First, the effect of two shape parameters $(q, \alpha_c)$ in MQ-RBF that used to create the RPIM shape functions is studied through this benchmark problem. The problem domain is represented by 196 regular nodes and 181 irregular nodes (as shown in Fig. 10). In the process of the study of $q$, $\alpha_c$ is fixed at 4.0, a circular local support

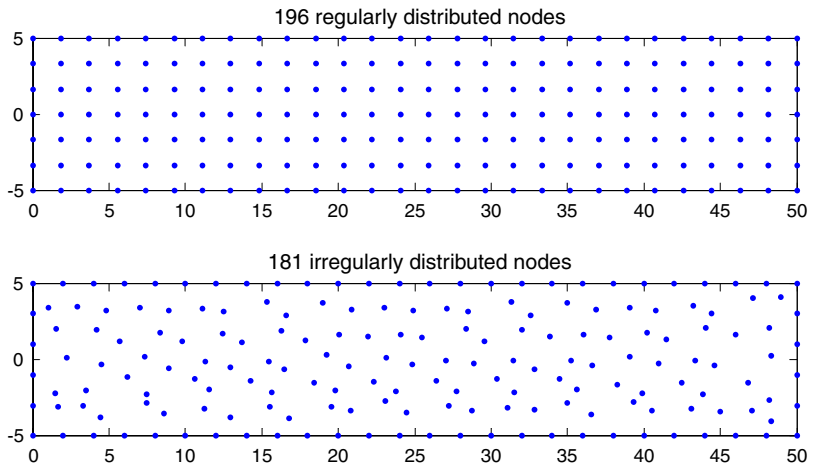


Fig. 10. Illustration of regular and irregular nodes distribution for the problem of cantilever beam.

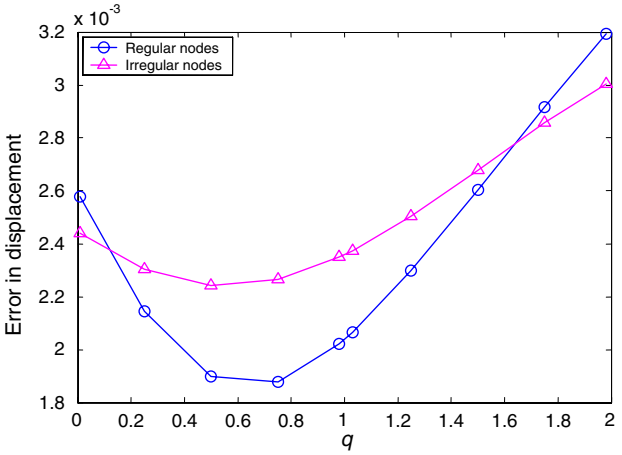


Fig. 11. Effect of parameter $q$ on the displacement results for the cantilever beam (196 and 181 nodes are used for regular and irregular nodes distribution; $\alpha_c = 4.0$ and $\alpha_s = 3.0$).

domain is adopted, and $\alpha_s$ is fixed at 3.0. For different values of $q$ (varies from 0.01 to 1.98), error of displacement defined in Eq. (45) is computed using the present NI-RPIM method and plotted in Fig. 11. Note that the value of $q$ must not be an integer number, because it will cause the failure of the RPIM due to the singularity of the moment matrix (Liu, 2002). Fig. 11 shows that a range of 0.4–1.0 for parameter $q$ will lead to better results for both regular and irregular nodes distribution. Based on previous study results (Liu, 2002), $q = 1.03$ was found good and hence is adopted in the present method. In the following study of effect of parameter $\alpha_c$, a circular support domain is used and $\alpha_s$ is fixed at 3.0. Value of $\alpha_c$ varies from 1.0 to 7.0 and the errors of displacement obtained using the present method are plotted in Fig. 12. The figure shows that a value of $\alpha_c$ around 4.0 will lead to better results for both regular and irregular nodes distributions. It is consistent with the previous conclusions obtained by other authors (Wang and Liu, 2002b; Liu et al., 2005b). Therefore $\alpha_c = 4.0$ is used in this work for the following problems.

### 5.3.2. Effect of dimension of the local support domain

The dimension of the local support domain controls the number of field nodes used in the RPIM shape function construction, and can affect the numerical results. Values of shape parameters are fixed as ($q = 1.03$, $\alpha_c = 4.0$), different values of $\alpha_s$ are examined and the displacement errors obtained for regular and irregular nodes distribution are plotted in Fig. 13, respectively. Based on this study, $\alpha_s$ of 2.5–3.5 that includes 12–40 field nodes provides good results and is used in this work.

### 5.3.3. Numerical results of the cantilever beam

The beam is studied using both the regular and irregular modes of nodes distribution (shown in Fig. 10). The numerical results of displacement in $y$ direction along the neutral line and the shear stress along the middle line are obtained using the present method with 196 regular and 181 irregular nodes distribution and plotted in Figs. 14 and 15, respectively. The pictures show that the numerical solutions of displacement and stress components are all in good agreement with the analytical ones and the mode of nodal distribution has little effect on the results.

### 5.3.4. Comparison study of convergence and efficiency

To study the properties of convergence and efficiency, the cantilever beam is studied using three models of regular nodes (85, 297 and 1105 nodes distribution). Four different methods are used in the analysis: the traditional FEM with 4-node quadrilateral element, the original RPIM with Gauss integration scheme, the NI-MLS method and the present NI-RPIM. For the RPIM using Gauss integration, $2 \times 2$ Gauss points are employed for each quadrilateral background cell. The NI-MLS is formulated using linear and quadratic polynomial basis functions, respectively, and they are labeled, respectively, as linear NI-MLS and quadratic

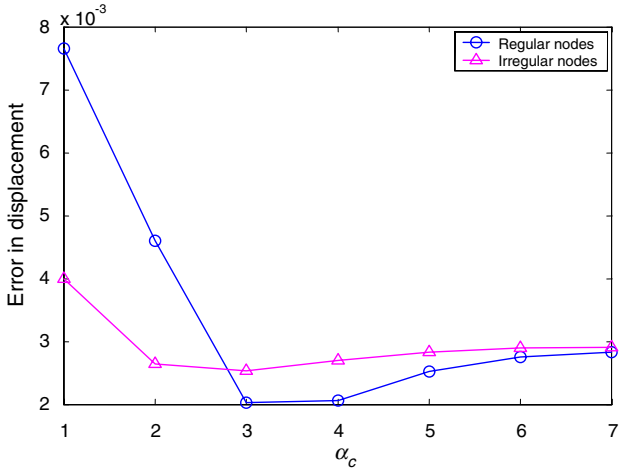


Fig. 12. Effect of parameter $\alpha_c$ on the displacement results for the cantilever beam (196 and 181 nodes are used for regular and irregular nodes distribution; $q = 1.03$ and $\alpha_s = 3.0$).

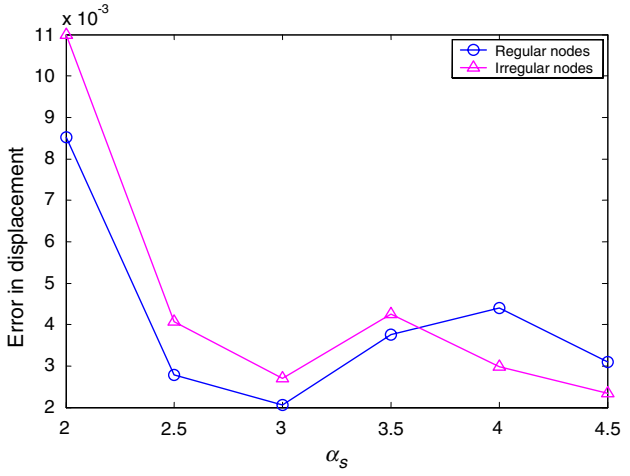


Fig. 13. Effect of dimension of the local support domain on the displacement results for the cantilever beam (196 and 181 nodes are used for regular and irregular nodes distribution; $\alpha_c = 4.0$ and $q = 1.03$).

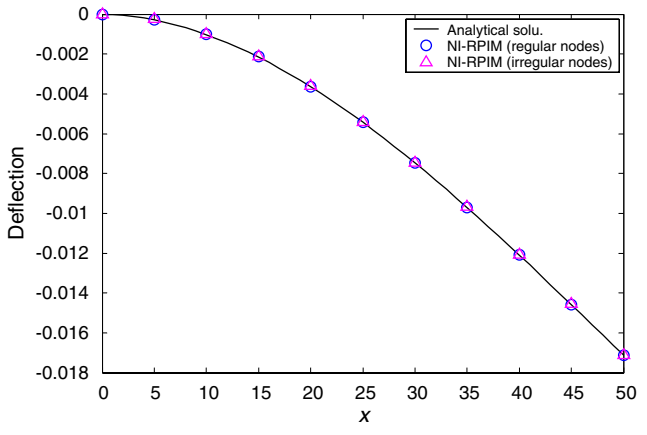


Fig. 14. Deflection distribution along the neutral line of the cantilever beam.

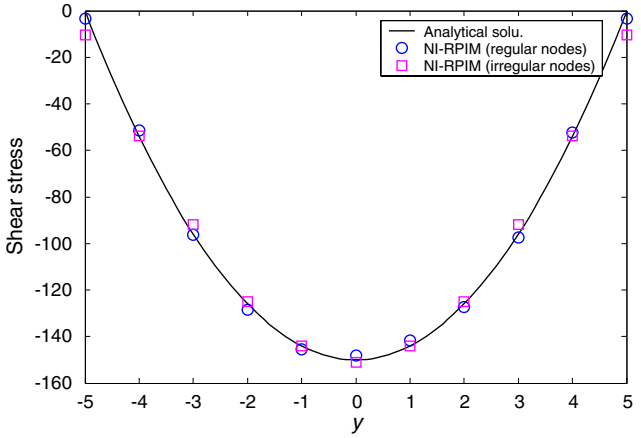


Fig. 15. Shear stress distribution along the line ($x = L/2$) of the cantilever beam.

NI-MLS in this work. The results of displacement and energy errors against $h$ are plotted in Fig. 16 for these four methods, where $h$ is the average nodal spacing for the nodes distribution. The picture shows that the RPIM, the quadratic NI-MLS, and the present NI-RPIM would be more accurate than the FEM and the linear NI-MLS. In Fig. 17, the errors of the numerical results obtained using these four methods are plotted against the CPU time consumed, which shows the performance of efficiency. It can be found that the three methods, i.e. the RPIM, the quadratic NI-MLS, and the NI-RPIM, are more efficient than the FEM. Compared with the original RPIM with Gauss integration, the NI-RPIM is more efficient when using the present simple nodal integration scheme.

### 5.4. An infinite plate with a hole

An infinite plate with a hole (a = 10 units) subjected to a tensile of 10 units is examined. Due to two-fold symmetry, only one quarter is modeled, as shown in Fig. 18. In the model, the analytical solutions of stress components are applied on the boundaries at $x = 50$ and $y = 50$. The essential boundary conditions are

$$u(x = 0) = 0 \quad (10 \leqslant y \leqslant 50); \qquad v(y = 0) = 0 \quad (10 \leqslant x \leqslant 50). \tag{58}$$

The analytical solution of this problem is used below (Timoshenko and Goodier, 1970),

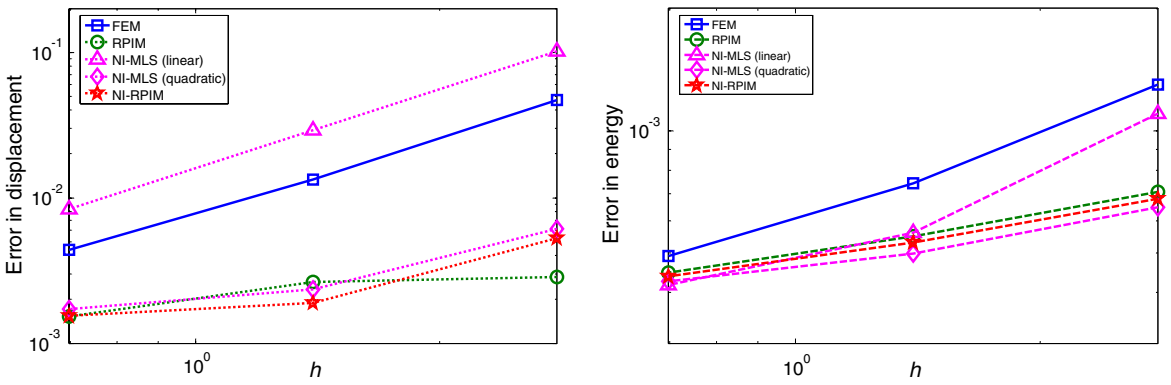


Fig. 16. Comparison of convergence of four different methods, i.e. the FEM, the RPIM, the NI-MLS and the NI-RPIM. (The cantilever beam is used for examination. In the FEM, 4-node quadrilateral element is used; in the RPIM, Gauss integration is adopted with the parameters of $\alpha_c = 4.0$, $q = 1.03$ and $\alpha_s = 3.0$; in the NI-MLS, linear and quadratic polynomial basis functions are both used with the cubic weight function; in the NI-RPIM, the present nodal integration technique is adopted with the parameters of $\alpha_c = 4.0$, $q = 1.03$ and $\alpha_s = 3.0$.)

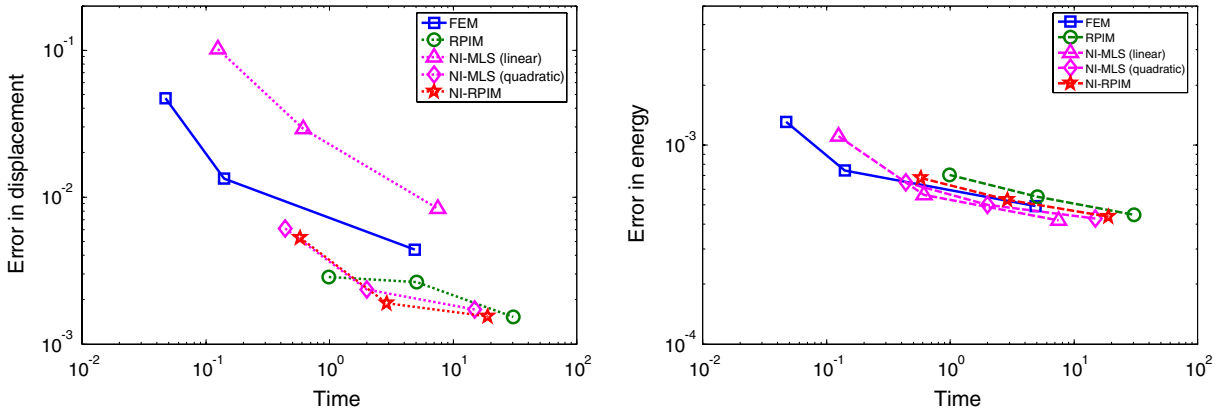


Fig. 17. Comparison of efficiency of four different methods, i.e. the FEM, the RPIM, the NI-MLS and the NI-RPIM. (The cantilever beam is used for examination. In the FEM, 4-node quadrilateral element is used; in the RPIM, Gauss integration is adopted with the parameters of $\alpha_c = 4.0$, $q = 1.03$ and $\alpha_s = 3.0$; in the NI-MLS, linear and quadratic polynomial basis functions are both used with the cubic weight function; in the NI-RPIM, the present nodal integration technique is adopted with the parameters of $\alpha_c = 4.0$, $q = 1.03$ and $\alpha_s = 3.0$.)

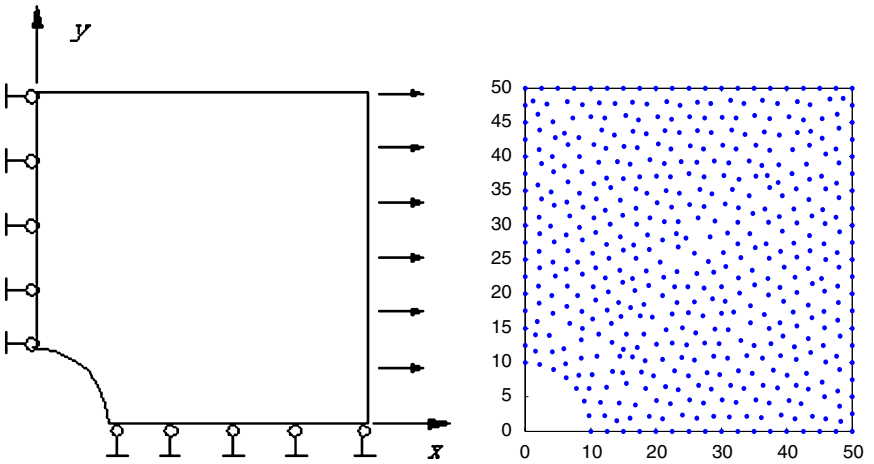


Fig. 18. A quarter model of an infinite plate with a hole subjected to a tensile force and the illustration of nodes distribution of 489 nodes.

$$u_r = \frac{T_x}{4\mu}\left\{r\left[\frac{(\kappa-1)}{2}+\cos(2\theta)\right]+\frac{a^2}{r}\left[1+(1+\kappa)\cos(2\theta)\right]-\frac{a^4}{r^3}\cos(2\theta)\right\} \tag{59}$$

$$u_\theta = \frac{T_x}{4\mu}\left[(1-\kappa)\frac{a^2}{r}-r-\frac{a^4}{r^3}\right]\sin(2\theta), \tag{60}$$

where

$$\mu = \frac{E}{2(1+v)}, \quad \kappa = \begin{cases} 3-4v & \text{Plane strain,} \\ \frac{3-v}{1+v} & \text{Plane stress,} \end{cases} \tag{61}$$

$$\sigma_{xx} = T_x\left\{1-\frac{a^2}{r^2}\left[\frac{3}{2}\cos(2\theta)+\cos(4\theta)\right]+\frac{3a^4}{2r^4}\cos(4\theta)\right\}, \tag{62}$$

$$\sigma_{yy} = -T_x\left\{\frac{a^2}{r^2}\left[\frac{1}{2}\cos(2\theta)-\cos(4\theta)\right]+\frac{3a^4}{2r^4}\cos(4\theta)\right\}, \tag{63}$$

$$\sigma_{xy} = -T_x\left\{\frac{a^2}{r^2}\left[\frac{1}{2}\sin(2\theta)+\sin(4\theta)\right]-\frac{3a^4}{2r^4}\sin(4\theta)\right\}. \tag{64}$$

In this study, the problem is analyzed as plane stress and the domain is represented by 489 irregularly distributed nodes (shown in Fig. 18). The numerical displacement solutions along two boundary lines ($x = 0; y = 0$) and the normal stress solutions along the line ($x = 0$) are plotted in Figs. 19 and 20, respectively. The figures show that the numerical solutions obtained using the present method are in a very good agreement with the analytical solutions also for this benchmark problem.

### 5.5. Internal pressurized hollow cylinder

A hollow cylinder subjected to internal pressure (shown in Fig. 21) is also analyzed. The cylinder is of internal radius $a = 10$, outer radius $b = 25$, and internal pressure $p = 100$ units. Plain strain condition is considered and the analytical solutions can be written as (Timoshenko and Goodier, 1970),

$$u_r = \frac{pa^2}{E(b^2 - a^2)r}[(1 - v)r^2 + (1 + v)b^2], \tag{65}$$

$$\sigma_r = \frac{a^2 p}{b^2 - a^2}\left(1 - \frac{b^2}{r^2}\right), \tag{66}$$

$$\sigma_\theta = \frac{a^2 p}{b^2 - a^2}\left(1 + \frac{b^2}{r^2}\right). \tag{67}$$

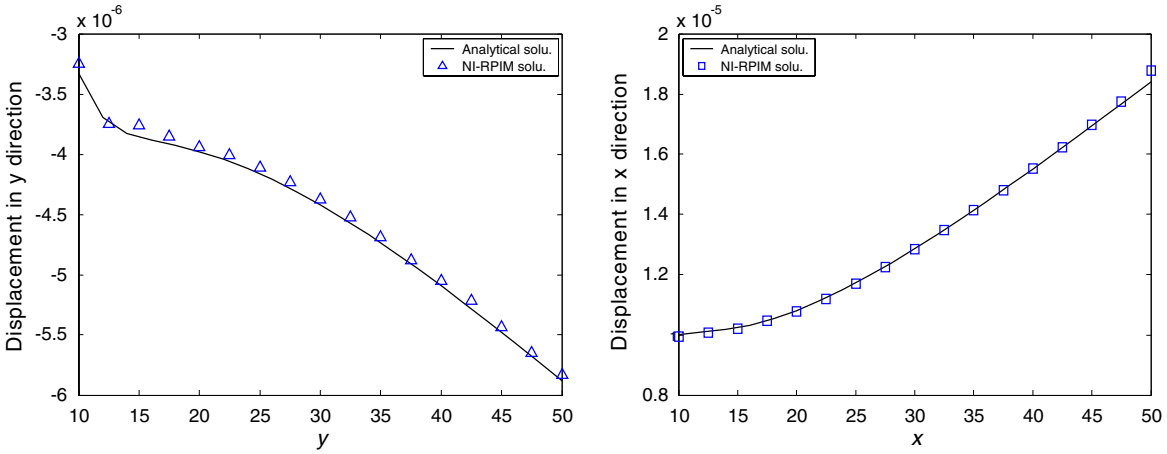


Fig. 19. Displacement distribution along two boundary lines ($x = 0$ and $y = 0$).

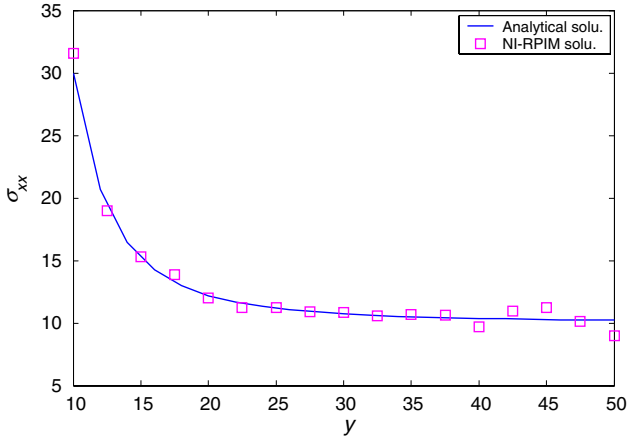


Fig. 20. Stress distribution along the boundary line ($x = 0$).

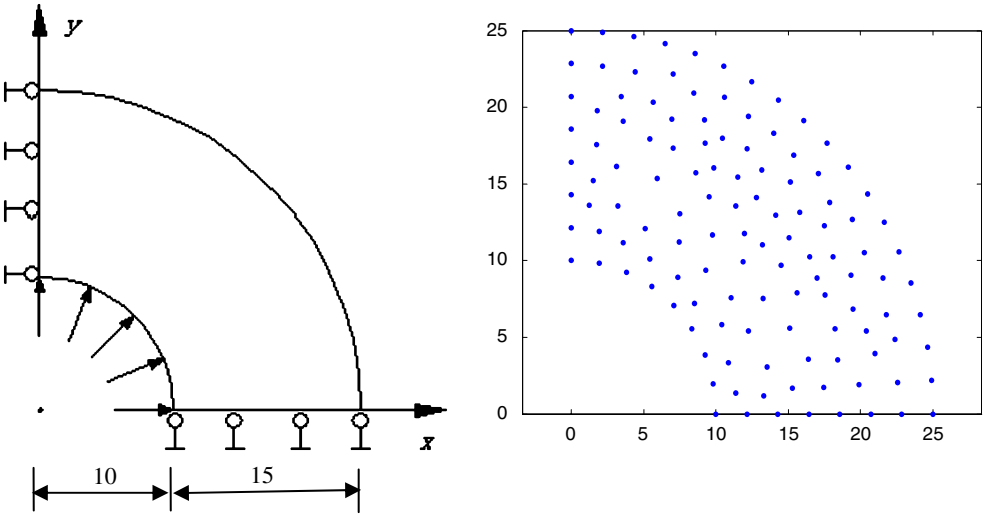


Fig. 21. A quarter model of hollow cylinder subjected to internal pressure and the illustration of nodes distribution of 123 nodes.

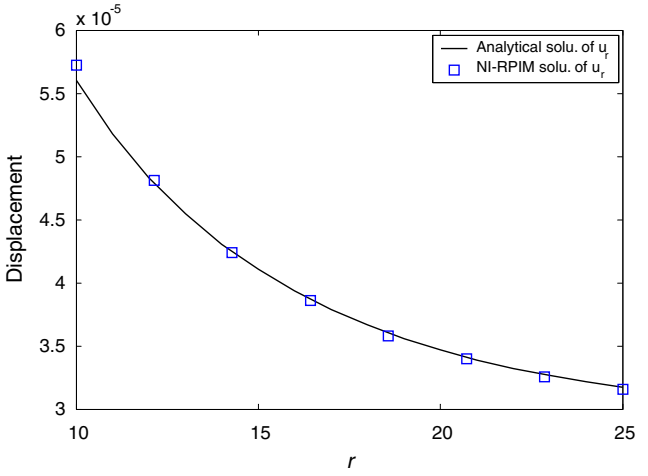


Fig. 22. Displacement distribution along the boundary line ($x = 0$).

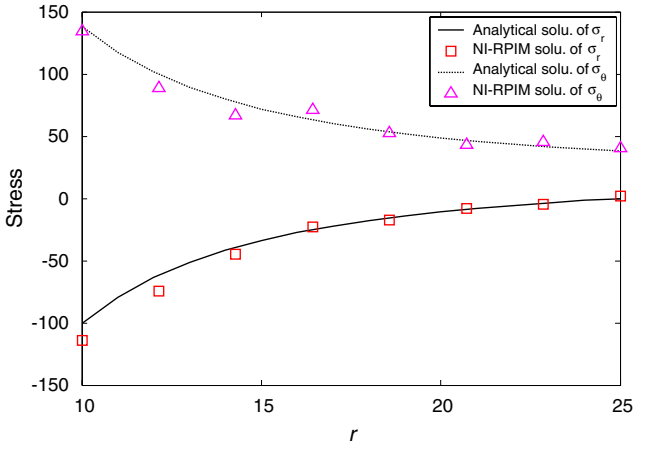


Fig. 23. Stress distribution along the boundary line ($x = 0$).

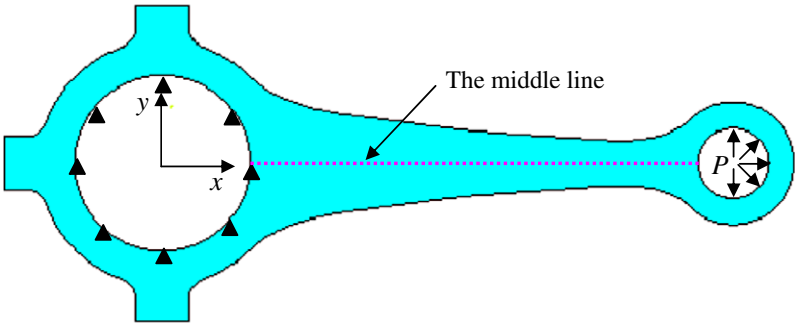


Fig. 24. Model of the connecting rod used in automobiles.

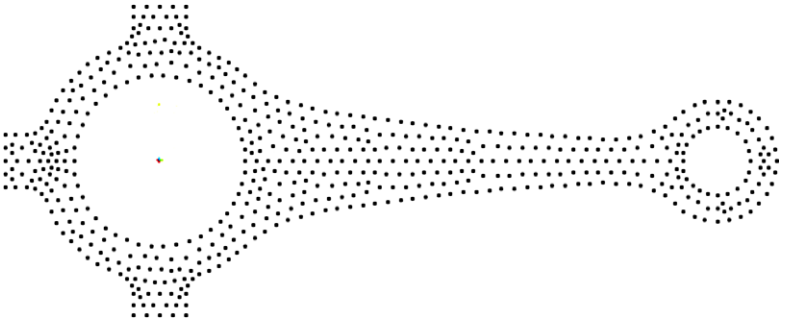

Fig. 25. Nodal distribution for the connecting rod problem.

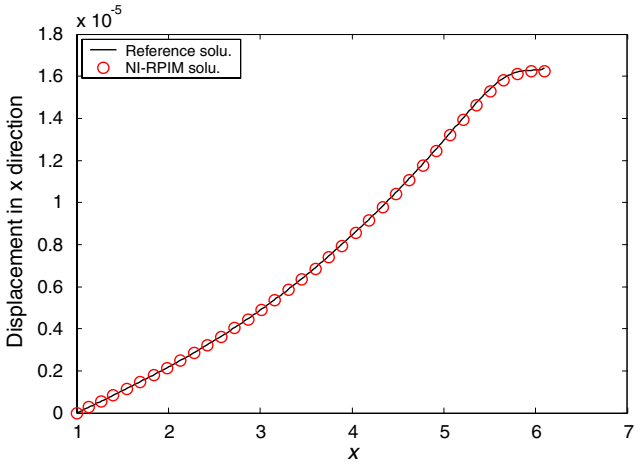


Fig. 26. Displacement distribution along the middle line.

The problem is discretized by 123 irregularly distributed nodes (shown in Fig. 21). The numerical solutions using the present method are plotted in Figs. 22 and 23. The figures show that both the displacement and stress solutions, obtained using the present NI-RPIM method, coincide well with the analytical ones.

### 5.6. An automotive part: connecting rod

Finally, a typical connecting rod used in automobiles, as shown in Fig. 24, is studied using the present method. The value of the pressure is 100 units. As shown in Fig. 25, the rod is discretized using 592 irregularly

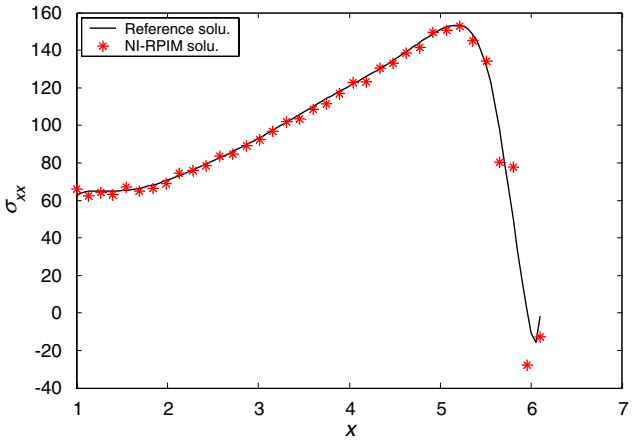


Fig. 27. Normal stress ($\sigma_{xx}$) distribution along the middle line.

distributed nodes. Along the middle dashed line (shown in Fig. 24), the displacement and the normal stress components in $x$ direction of the nodes are plotted. Because the exact solution is not available, the reference solution is obtained using the ANSYS with a very fine mesh of 7756 6-node triangular elements. The numerical solutions obtained using the present method are plotted in Figs. 26 and 27 with the reference ones. The figures show that, the present method can obtain very good results of both the displacement and stress components.

## 6. Conclusions

In this work, a nodal integration technique for meshfree radial point interpolation method (NI-RPIM) is proposed. This method employs radial basis functions (RBFs) augmented with polynomials to construct shape functions. Galerkin weak form is adopted and a nodal integration scheme based on Taylor series extension is introduced to perform the numerical integration. Some numerical examples are examined and the effects of shape parameters as well as the dimension of the local support domains are investigated. From the research work, the following conclusions can be drawn.

- Shape functions generated using RBFs augmented with polynomials possess the Delta property, which allows straightforward imposition of point essential boundary conditions.
- Based on the study of examples in this paper and the previous works on RPIM, $q = 1.03$ and $\alpha_c = 4$ are recommended for NI-RPIM.
- For the circular support domain, $\alpha_s = 2.5$–$3.5$ which includes 12–40 field nodes are suggested.
- The benchmark numerical examples show that the results obtained using the present nodal integration technique is accurate and stable.
- Compared with the traditional FEM, the NI-RPIM will be more accurate and more efficient; compared with the original RPIM adopting Gauss integration scheme, the NI-RPIM can achieve higher convergence rate and efficiency; compared with the NI-MLS, the NI-RPIM performs much better than the linear NI-MLS and is almost in the same level of performance of quadratic NI-MLS.

## References

Atluri, S.N., Zhu, T., 1998. A new meshless local Petrov-Galerkin (MLPG) approach in computational mechanics. Computational Mechanics 22, 117–127.

Belytschko, T., Beissel, S., 1996. Nodal integration of the element-free Galerkin method. Computer Methods in Applied Mechanics and Engineering 139, 49–74.

Belytschko, T., Lu, Y.Y., Gu, L., 1994. Element-free Galerkin methods. International Journal for Numerical Methods in Engineering 37, 229–256.

Chen, J.S., Wu, C.T., Yoon, S., You, Y., 2001. A stabilized conforming nodal integration for Galerkin mesh-free methods. International Journal for Numerical Methods in Engineering 50, 435–466.

Ferziger, J.H., Peric, M., 1999. Computational Methods for Fluid Dynamics. Springer, Berlin, Germany.

Golberg, M.A., Chen, C.S., Bowman, H., 1999. Some recent results and proposals for the use of radial basis functions in the BEM. Engineering Analysis with Boundary Elements 23, 285–296.

Hardy, R.L., 1990. Theory and applications of the multiquadrics-biharmonic method (20 years of discovery 1968–1988). Computers & Mathematics with Applications 19, 163–208.

Liszka, T., Orkisz, J., 1980. The finite difference methods at arbitrary irregular grids and its applications in applied mechanics. Computers & Structures 11, 83–95.

Liu, G.R., 2002. Meshfree Methods: Moving Beyond the Finite Element Method. CRC Press, Boca Raton, USA.

Liu, G.R., Gu, Y.T., 2001. A point interpolation method for two-dimensional solids. International Journal for Numerical Methods in Engineering 50, 937–951.

Liu, G.R., Gu, Y.T., 2003. A meshfree method: meshfree weak–strong (MWS) form method, fro 2-D solids. Computational Mechanics 33 (1), 2–14.

Liu, G.R., Gu, Y.T., 2005. An Introduction to Meshfree Methods and Their Programming. Springer, Dordrecht, The Netherlands.

Liu, G.R., Li, Y., Dai, K.Y., Luan, M.T., Xue, W., 2006. A linearly conforming RPIM for 2D solid mechanics. International Journal of Computational Methods (in press).

Liu, G.R., Liu, M.B., 2003. Smoothed Particle Hydrodynamics – A Meshfree Practical Method. World Scientific, Singapore.

Liu, G.R., Wu, Y.L., Ding, H., 2004. Meshfree weak–strong (MWS) from method and its application to incompressible flow problems. International Journal for Numerical Methods in Fluids 46, 1025–1047.

Liu, G.R., Zhang, G.Y., Dai, K.Y., Wang, Y.Y., Zhong, Z.H., Li, G.Y., Han, X., 2005a. A linearly conforming point interpolation method (LC-PIM) for 2D solid mechanics problems. International Journal of Computational Methods 2 (4), 645–665.

Liu, G.R., Zhang, G.Y., Gu, Y.T., Wang, Y.Y., 2005b. A meshfree radial point interpolation method (RPIM) for three-dimensional solids. Computational Mechanics 36 (6), 421–430.

Liu, W.K., Chen, Y., Jun, S., Chen, J.S., Belytschko, T., Pan, C., Uras, R.A., Chang, C.T., 1996. Overview and applications of the reproducing kernel particle methods. Archives of Computational Methods in Engineering State of the Art Reviews 3, 3–80.

Liu, W.K., Ong, J.S., Uras, R.A., 1985. Finite element stabilization matrices-a unification approach. Computer Methods in Applied Mechanics and Engineering 53, 13–46.

Lucy, L., 1977. A numerical approach to testing the fission hypothesis. The Astronomical Journal 82, 1013–1024.

Nagashima, T., 1999. Node-by-node meshless approach and its applications to structural analysis. International Journal for Numerical Methods in Engineering 46, 341–385.

Powell, M.J.D., 1992. The theory of radial basis function approximation in 1990. In: Light, F.W. (Ed.), Advances in Numerical Analysis, pp. 303–322.

Schaback, R., 1994. Approximation of polynomials by radial basis functions. In: Laurent, P.J., Mehaute, Le., Schumaker, L.L. (Eds.), Wavelets, images and surface fitting, Wellesley, MA, pp. 459–466.

Timoshenko, S.P., Goodier, J.N., 1970. Theory of Elasticity, third ed. McGraw-hill, New York.

Wang, J.G., Liu, G.R., 2002a. A point interpolation meshless method based on radial basis functions. International Journal for Numerical Methods in Engineering 54, 1623–1648.

Wang, J.G., Liu, G.R., 2002b. On the optimal shape parameters of radial basis functions used for 2-D meshless methods. Computer Methods in Applied Mechanics and Engineering 191, 2611–2630.

Wendland, H., 1998. Error estimates for interpolation by compactly supported radial basis functions of minimal degree. Journal of Approximation Theory 93, 258–396.